Mon. Not. R. Astron. Soc. **000**, 1–13 (2012) Printed June 4, 2014 (MN LATEX style file v2.2)

Thermal emission of neutron stars with internal heaters

A. D. Kaminker[1], A. A. Kaurov[2], A. Y. Potekhin[1,3,4] and D. G. Yakovlev[1]
[1] *Ioffe Physical-Technical Institute, Politekhnicheskaya 26, Saint Petersburg, 194021, Russia*
[2] *Department of Astronomy and Astrophysics, University of Chicago, Chicago IL 60637, USA*
[3] *Central Astronomical Observatory of RAS at Pulkovo, Pulkovskoe Shosse 65, Saint Petersburg, 196140, Russia*
[4] *Isaac Newton Institute of Chile, St. Petersburg Branch, Russia*

arXiv:1406.0723v1 [astro-ph.HE] 3 Jun 2014

Accepted 2013 xxxx. Received 2013 xxxx; in original form 2013 xxxx

ABSTRACT

Using 1D and 2D cooling codes we study thermal emission from neutron stars with steady state internal heaters of various intensities and geometries (blobs or spherical layers) located at different depths in the crust. The generated heat tends to propagate radially, from the heater down to the stellar core and up to the surface; it is also emitted by neutrinos. In local regions near the heater the results are well described with the 1D code. The heater's region projects onto the stellar surface forming a hot spot. There are two heat propagation regimes. In the first, *conduction outflow* regime (realized at heat rates $H_0 \lesssim 10^{20}$ erg cm^{-3} s^{-1} or temperatures $T_{\rm h} \lesssim 10^9$ K in the heater) the thermal surface emission of the star depends on the heater's power and neutrino emission in the stellar core. In the second, *neutrino outflow* regime ($H_0 \gtrsim 10^{20}$ erg cm^{-3} s^{-1} or $T_{\rm h} \gtrsim 10^9$ K) the surface thermal emission becomes independent of heater's power and the physics of the core. The largest (a few per cent) fraction of heat power is carried to the surface if the heater is in the outer crust and the heat regime is intermediate. The results can be used for modeling young cooling neutron stars (prior to the end of internal thermal relaxation), neutron stars in X-ray transients, magnetars and high-B pulsars, as well as merging neutron stars.

Key words: dense matter — stars: neutron – neutrinos.

1 INTRODUCTION

Neutron stars manifest themselves in different ways (e.g. Haensel, Potekhin & Yakovlev 2007). They are born hot in supernova explosions but gradually cool down due to neutrino emission from the entire stellar body and due to photon emission from the surface. Thermal radiation from isolated cooling neutron stars carries important information on internal structure of these stars. Moreover, different mechanisms of extra energy release can operate inside the neutron stars (e.g., Page, Geppert & Weber 2006). For instance, an extra heating can be provided by viscous friction in the presence of differential rotation (e.g., Chirenti, Skakala & Yoshida 2013), slow chemical equilibration of the star in the course of its evolution (Petrovich & Reisenegger 2010), Ohmic decay of internal magnetic fields (in ordinary neutron stars and magnetars; e.g., Viganò et al. 2013 and references therein), nuclear reactions in deep layers of the star's crust (Haensel & Zdunik 1990, 2008; Brown, Bildsten & Rutledge 1998), or glitches (e.g., Espinoza et al. 2011).

In this paper we study possible manifestations of the internal heaters in producing thermal surface radiation. We will model the heaters phenomenologically as some hot quasistationary heat sources of different size and intensity, located in various places of the neutron star crust, and see how much heat can diffuse to the surface and be emitted as thermal radiation. The results will be helpful for constraining the properties of the heater and its dense environment from observations of thermal radiation from neutron stars.

We have already studied the formulated problem in papers devoted to magnetars, i.e., neutron stars with very strong magnetic fields $B \gtrsim 10^{14}$ G (Kaminker et al. 2006, 2009) (hereafter Papers I and II, respectively). The aim was to explain quasistationary thermal emission of magnetars (e.g., Mereghetti 2008, 2013; Olausen & Kaspi 2014) by the presence of internal heaters. To this aim, we have used our generally relativistic 1D cooling code (Gnedin, Yakovlev & Potekhin 2001) with a phenomenological spherically symmetric heat layer in the neutron star crust. The results were summarized in Paper I for heat-blanketing envelopes made of iron and in Paper II for magnetar models with accreted heat-blanketing envelopes. The description of heat transport in the stellar interior (under the heat blanketing envelope, at densities $\rho \gtrsim \rho_{\rm b} \sim 10^{10}$ g cm^{-3}) was approximate, because the temperature distribution in the interior was treated as spherically symmetric and the anisotropy of heat transport was neglected.

This paper is different from the previous ones in two

© 2012 RAS

respects. First, we supplement our 1D calculations by the calculations made with our new 2D code. This allows us to consider axially symmetric heaters and temperature distributions in the stellar interior. Second, we mainly focus on neutron stars without magnetic fields or with fields $B \lesssim 10^{12}$ G, which weakly affect thermal structure and evolution of the stars (e.g., Yakovlev & Pethick 2004). In this case our scheme of solving the heat transport problem in the stellar interior is more robust than in Papers I and II. Preliminary results of the present study have been published by Kaminker et al. (2012). We show that many observational manifestations of internal steady state heaters obtained for magnetars are also valid for ordinary neutron stars.

2 PHYSICS INPUT

We calculate thermal radiation from neutron stars with internal heaters using two cooling codes. First, we employ our usual 1D fully relativistic cooling code (Gnedin, Yakovlev & Potekhin 2001; also see Papers I and II) with a spherically symmetric heater. Second, we use a new simplified 2D cooling code (Kaminker et al. 2012) with an axially symmetric heater, like a hot blob within the neutron star crust. The two codes allow us to follow the cooling more reliably.

Both codes simulate cooling of an initially hot star via neutrino emission from the entire stellar body and via thermal emission of photons from the surface. To facilitate calculations we use the standard procedure of dividing the star in the bulk interior and a thin outer heat-blanketing envelope (Gudmundsson, Pethick & Epstein 1983). The envelope extends from the radiative surface to the layer of the density $\rho_{\rm b} = 10^{10}$ g cm^{-3}; typically it has a thickness $\sim$ 100 m and mass $\lesssim 10^{-6}\,M_\odot$. We consider the ground-state composition of the matter according to Rüster, Hempel & Schaffner-Bielich (2006). The cooling results for this composition are almost the same as those obtained with the previous models of the ground state matter (e.g., Haensel et al. 2007) or purely iron heat blankets. The neutron drip density in the crust for all equations of state (EOSs) used in this paper is $\rho_d \approx 4 \times 10^{11}$ g cm^{-3}.

The internal structure of neutron stars can be regarded as temperature-independent (e.g., Haensel et al. 2007). The 1D code solves the *thermal balance* and *thermal transport* equations in the entire bulk interior (the crust and the core) in a spherically symmetric approximation, as described in Gnedin et al. (2001).

Our new 2D code solves the thermal balance and thermal transport equations in the *axially symmetric* approximation (see Sect. 3.1 of Aguilera, Pons & Miralles 2008) in the bulk of the crust in a locally flat reference frame. In the latter case we calculate all relevant quantities (temperature T, heat flux $\boldsymbol{F}$, neutrino emissivity Q_ν [erg cm^{-3} s^{-1}], etc.) as functions of radial coordinate r, Schwarzschild time t, and a polar angle θ with respect to the symmetry axis. The effects of General Relativity are taken into account by redshifting the results for a distant observer.

The stellar core in the 2D code is treated as isothermal and included approximately by introducing the crust-core boundary conditions. These conditions require the temperature over the boundary to be isothermal, $T = T_{\rm cc}$, and the generally relativistic equation of the core cooling to be satisfied, $dT_{\rm cc}^\infty/dt = -L_{\nu{\rm core}}^\infty(T_{\rm cc}^\infty)/C_{\rm core}^\infty(T_{\rm cc}^\infty)$. Here $L_{\nu{\rm core}}^\infty(T_{\rm cc}^\infty)$ and $C_{\rm core}^\infty(T_{\rm cc}^\infty)$ are, respectively, the neutrino luminosity and heat capacity of the isothermal core redshifted for a distant observer, e.g., Gnedin et al. (2001); $T_{\rm cc}^\infty$ is the redshifted $T_{\rm cc}$. The function $L_{\nu{\rm core}}^\infty(T_{\rm cc}^\infty)/C_{\rm core}^\infty(T_{\rm cc}^\infty)$ is calculated for a given neutron star model in a standard way. Similar simplified cooling models have been introduced earlier (e.g., Fortin et al. 2010).

Table 1. Masses M, radii R and central densities in units of 10^{14} g cm^{-3}, $\rho_{\rm c14}$, for neutron star models with the toy-model EOS SC+HHJ (for short, HHJ) and realistic EOS BSk21 (for short, BSk); see text.

Star model	$M/M_\odot$		R (km)		$\rho_{\rm c14}$	
	HHJ	BSk	HHJ	BSk	HHJ	BSk
Maximum mass	2.16	2.28	10.84	11.07	24.5	22.9
Fast cooler	1.85		12.32	12.46	11.34	9.98
Durca onset	1.77	1.57	12.46	12.58	10.50	8.09
Standard cooler	1.4		12.74	12.57	7.78	7.30

The specific heat capacity c_v in the core is calculated as the sum of contributions of strongly degenerate relativistic electrons and nucleons according to Yakovlev, Levenfish & Shibanov (1999). In the crust, the contribution of the lattice of atomic nuclei (Baiko, Potekhin & Yakovlev 2001) is added to those of free neutrons and electrons. The heat conductivity in the crust is mainly regulated by electron-ion scattering. For the isotropic case considered here, it is given in Potekhin et al. (1999). The neutrino emissivity Q_ν is taken from Yakovlev et al. (2001). Unlike the earlier works (e.g., Gudmundsson et al. 1983; Potekhin et al. 1997, 2003), we include neutrino emission in the heat-blanketing envelope, which can be important at high effective temperatures. In this case, the radial flux F_r is not constant through the heat-blanketing envelope. Therefore, both the effective surface temperature $T_{\rm s}$ and the flux value $F_r = F_{\rm b}$ at $\rho_{\rm b}$, have been simultaneously determined for a given temperature $T_{\rm b}$ by integration of a system of stationary equations of hydrostatic balance, thermal balance and thermal transport in the blanketing envelope, as described in Potekhin et al. (2007). The boundary conditions at $\rho = \rho_{\rm b}$ implied the continuity of T and F_r.

As will be shown below, our basic results depend on the employed EOS only weakly. For this reason, most of our calculations are performed with the use of a toy-model EOS, following Papers I and II. Specifically, in the neutron-star core we employ the simple parametrization of the energy $\mathcal{E}$ per nucleon that was constructed by Heiselberg & Hjorth-Jensen (1999) (hereafter HHJ),

$$\mathcal{E} = \mathcal{E}_0 u\,\frac{u-2-s}{1+su} + S_0 u^\gamma (1-2x_{\rm p})^2. \qquad (1)$$

Here, $u = n/n_0$; n is the baryon density; $n_0 = 0.16$ fm^{-3}, $\mathcal{E}_0$ and S_0 are, respectively, the baryon density, nucleon energy, and symmetry energy at saturation; $x_{\rm p}$ is the proton fraction (among baryons); s and γ are additional parameters. Following HHJ, we keep $\mathcal{E}_0 = 15.8$ MeV and $S_0 = 32$ MeV, but treat s and γ as free parameters. We denote this parametrization as HHJ(s,γ). In the attempt to fit the EOS

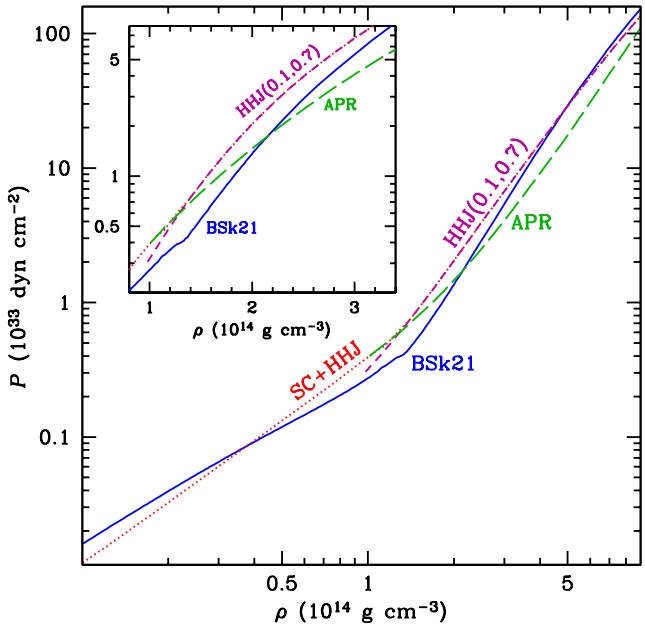

Figure 1. EOS models for the inner crust and the core: APR (long-dashed line) and HHJ(0.1,0.7) (short-dashed line) in the core, interpolated SC+HHJ (dotted line) and unified BSk21 (solid line) in the core and crust. The inset shows the same EOSs in a restricted range of densities.

by Akmal, Pandharipande & Ravenhall (1998), HHJ took $s = 0.2$ and $\gamma = 0.6$. Gusakov et al. (2005) studied cooling of neutron stars with the EOSs HHJ(0.2,γ) for three values of $\gamma = 0.6$, 0.575 and 0.643, and denoted these models as APR I, II and III, respectively. The latter model was also adopted in Papers I and II.

However, the HHJ parametrization is inaccurate in reproducing the original EOS of Akmal et al. (1998). For instance, all three HHJ parametrizations of Gusakov et al. (2005) give maximum neutron-star masses $M_{\rm max} \approx 1.9\,M_\odot$, significantly lower than the value $2.2\,M_\odot$ for the true APR EOS. It is lower than the value $M = 2.0\,M_\odot$ obtained in the modern observations of neutron stars (Demorest et al. 2010; Antoniadis et al. 2013). Therefore, in the present study we use the model HHJ(0.1,0.7) with $M_{\rm max} = 2.16\,M_\odot$ (Table 1). In the inner crust at $\rho_{\rm b} < \rho < \rho_{\rm cc}$, where $\rho_{\rm cc}$ refers to the crust-core boundary (e.g., $\rho_{\rm cc} = 1.3 \times 10^{14}$ g cm^{-3} according to Pearson et al. 2012), we match HHJ(0.1,0.7) with the "smooth composition" (SC) EOS described by Haensel et al. (2007). In practical calculations, we apply a spline-like matching between HHJ(0.1,0.7) and SC EOS in a range of densities near $\rho_{\rm cc}$. We denote this combined EOS as "SC+HHJ" (see Fig. 1).

In order to check the sensitivity to the EOS model, we compare the results obtained with the SC+HHJ EOS and analogous results obtained with the analytical representation of the realistic BSk21 EOS. This model belongs to a family of EOSs based on nuclear energy-density functionals, labelled BSk, which are derived from generalized Skyrme interaction functionals supplemented with several correction terms. Unlike APR and HHJ, the BSk EOSs are unified. It means that they can be used not only for the homogeneous nucleon-lepton matter in the stellar core, but also in the crust. The Skyrme parameters of the underlying energy-density functionals were fitted by Goriely, Chamel, & Pearson (2010) taking into account experimental and theoretical constraints on nuclear matter and neutron matter. Potekhin et al. (2013) derived analytical parametrizations of three BSk EOSs (BSk19, 20, and 21).

Table 2. Four models (a)–(d) of heater positions $\rho_1 \leqslant \rho \leqslant \rho_2$ in 1.4 and $1.85\,M_\odot$ stars

M:	1.4 & $1.85\,M_\odot$	$1.4\,M_\odot$	$1.85\,M_\odot$
label	ρ_1 (g cm^{-3})	ρ_2 (g cm^{-3})	ρ_2 (g cm^{-3})
(a)	3.2×10^{10}	9.20×10^{10}	9.34×10^{10}
(b)	3.2×10^{11}	1.60×10^{12}	1.60×10^{12}
(c)	3.2×10^{12}	1.27×10^{13}	1.26×10^{13}
(d)	3.2×10^{13}	5.47×10^{13}	5.39×10^{13}

BSk21 reproduces the EOS labelled "V18" in Li & Schulze (2008). This EOS model is selected, because it provides comfortably large $M_{\rm max} = 2.28\,M_\odot$ to accommodate observations, is most consistent with the experimental constraints (see Fig. 1 of Potekhin et al. 2013 and the discussion therein), and has a powerful predictive ability for properties of heavy neutron-rich nuclides (e.g., Wolf et al. 2013). A comparison of the EOSs APR, HHJ(0.1,0.7), SC+HHJ, and BSk21 is given in Fig. 1.

We will use two neutron star models, with $M = 1.4\,M_\odot$ and $1.85\,M_\odot$ (Table 1). The former is an example of a star with the standard (not too strong) neutrino emission in the core, mainly the modified Urca process in a non-superfluid star. The latter model is an example of a star whose neutrino emission is enhanced by the direct Urca (briefly Durca) process (Lattimer et al. 1991) in a small inner kernel (1.05×10^{15} g cm^{-3} $< \rho <$ 1.134×10^{15} g cm^{-3} for SC+HHJ or 8.09×10^{14} g cm^{-3} $< \rho <$ 9.98×10^{14} g cm^{-3} for BSk21). For simplicity, we consider non-superfluid neutron star models. Superfluidity would affect the neutrino emission and heat capacity of the neutron star core; it would further complicate our analysis. Detailed studies of superfluid neutron stars with internal heating can be subject of a separate project.

Following Papers I and II, we introduce an internal phenomenological heat source located in a layer at $\rho_1 \leqslant \rho \leqslant \rho_2$. The heat rate H [erg cm^{-3} s^{-1}] is taken in the form

$$H = H_0\,\Theta(\rho)\,\exp(-t/\tau), \qquad (2)$$

where H_0 is the initial (age $t = 0$) heat intensity; $\Theta(\rho) \approx 1$ in the middle of density interval $\rho_1 < \rho < \rho_2$, and $\Theta(\rho)$ vanishes outside this interval; and τ is the e-folding decay time of the heat release. We treat H_0, ρ_1, ρ_2, and τ as free input parameters. In the 2D calculations, we also assume that Θ is independent of θ at $\theta < \theta_0$ and $\Theta(\rho,\theta) = 0$ at $\theta \geqslant \theta_0$. Then the heater looks like a hot blob of angular size θ_0. The total heat power W^∞ (erg s^{-1}), redshifted for a distant observer, is

$$W^\infty(t) = \int {\rm d}V\, {\rm e}^{2\Phi}\, H, \qquad (3)$$

where ${\rm d}V$ is a proper volume element (as before, redshifted

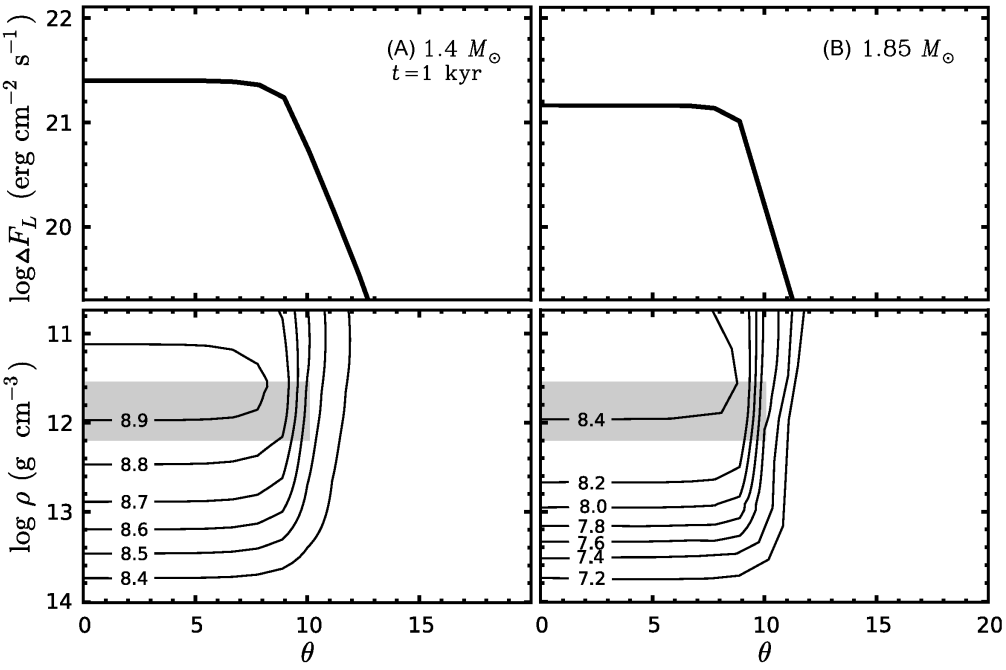

Figure 2. *Upper panels*: Excess thermal flux density ΔF_L through the neutron star surface produced by the 2D heater of type 2(b) in notations of Tables 3 and 2, with $\theta_0 = 10°$, in the star of mass (A) $1.4\,M_\odot$ (left) and (B) $1.85\,M_\odot$ (right) at $t = 1$ kyr, as a function of polar angle θ. *Lower panels*: Lines of constant $\log_{10} T$ (numbers next to curves) within the star on the plane (θ, ρ); shaded domains locate the heater.

Table 3. Five levels 0,...4 of heat intensity H_0 used in calculations

Label	0	1	2	3	4
H_0 (erg s^{-1} cm^{-3})	0	$10^{18.5}$	$10^{19.5}$	$10^{20.5}$	$10^{21.5}$

quantities are marked by the index ∞). In calculations, we used the smooth function $\Theta(\rho)$ as discussed in Paper II. An exact shape of $\Theta(\rho)$ in Eq. (2) is unimportant for the surface temperature distribution, provided the total heat power W^∞ is fixed (Paper II).

For each M we take four positions of the heater (labelled "(a)–(d)") with ρ_1 and ρ_2 given in Table 2; the bottom densities ρ_2 are chosen in such a way that all the heaters (a)–(d) have the same power W^∞ at the same heat intensity H_0 (in a star of given mass). As seen from Table 2, the values of ρ_2 for $1.4\,M_\odot$ and $1.85\,M_\odot$ stars are very close (non-distinguishable in the figures presented below).

In numerical examples we will often use five levels of heat intensity H_0 labelled as 0,...,4. Level 0 corresponds to no heating, whereas the other four levels refer to progressively stronger heating (Table 3). As in Papers I and II, we set $\tau = 5 \times 10^4$ yr and consider the case of $t \ll \tau$ (as discussed below, exact values of t and τ are unimportant for our analysis). Therefore, well within the heater ($\rho_1 \ll \rho \ll \rho_2$; $\theta < \theta_0$) at $t \ll \tau$ we have $H(\rho, \theta, t) \approx H_0$.

The total heat power W^∞ is usually most important in applications. Nevertheless, it is H_0 which determines thermal state of the heater, as has been analyzed in Papers I and II (e.g. Fig. 5 in Paper I), and will be discussed here in Sects. 4.1 and 4.2.

3 CALCULATIONS WITH THE 2D CODE

We have applied the 2D code to simulations of cooling neutron stars with the internal blob-like heater in the crust. We have used the EOS SC+HHJ and varied neutron star mass ($1.4\,M_\odot$ and $1.85\,M_\odot$; Table 1) as well as the parameters of the heater (H_0, ρ_1, ρ_2, θ_0; Tables 2, 3). We have calculated the density of the heat flux F_L emergent from a local part of the surface. It depends on t because the star cools down. However, it is instructive to introduce the excess heat flux density

$$\Delta F_L = F_L - F_{L0}, \qquad (4)$$

where F_{L0} is the heat flux for the star of the same age but without any heater. The excess flux ΔF_L appears to be robust, almost independent of neutron star age and cooling dynamics (as long as $t \ll \tau$). It describes the quasi-stationary thermal state of the star that is regulated by the heater itself and is independent of the cooling history; hereafter, we present the results obtained at $t = 10^3$ yr. These results depend on the stellar age as well as on the EOS model only slightly (see, e.g., Fig. 3 of Paper I, and Figs. 6 and 7 of Paper II, and discussion in these papers).

An example of 2D calculations is given in Fig. 2. The heater is placed in an upper part of the inner crust: model (b) in Table 2. The heat intensity is $H_0 = 10^{19.5}$ erg cm^{-3} s^{-1} (level 2 in Table 3), and the heater's angular size is $\theta_0 = 10°$. The left and right panels in Fig. 2 correspond to the stan-

dard and fast coolers, respectively. The upper panels show the excess thermal flux at the surface as a function of the polar angle θ. The bottom panels present lines of constant temperature T as a function of ρ and θ. The hatched regions on the (ρ, T)-plane are occupied by the heater. Here, the temperatures and surface fluxes are not redshifted.

One can see that the internal temperature under the heater (near the bottom of the inner crust) in the 1.85 $M_\odot$ star is drastically lower than in the 1.4 $M_\odot$ star. This is because of much stronger neutrino cooling (via the Durca process) from the core of the more massive star. Nevertheless the geometries of the temperature distributions, $T(\rho, \theta)$, and excess surface emissions, $\Delta F_L(\theta)$, look similar for both stars. One sees that the generated heat does not intend to spread along the surface but propagates almost radially from the heater up to the surface and down to the core. The excess heat flux produces a hot spot as a direct projection of the heater on the surface. The excess flux $\Delta F_L(\theta)$ is almost constant from $\theta = 0$ to $\theta \approx \theta_0 - 2^\circ$ and exponentially decreases at $\theta \gtrsim \theta_0$ with e-folding width $\lesssim 1^\circ$.

Similar results have been obtained by Pons & Rea (2012), who modelled heat outflow in a magnetar outburst near a magnetic pole with anisotropic heat conduction throughout the crust. The anisotropy becomes important in a strong magnetic field, which suppresses the electron heat transport across field lines. Here we see that the same radial heat propagation takes place even with isotropic conduction in the crust without magnetic field.

The important outcome of the present 2D calculations is that one can accurately model heat propagation in a local part of the heater using the 1D (radial) approximation. Note, however, that this conclusion does not apply in a strong magnetic field near the lines where the field is tangential to the surface, as discussed in Potekhin et al. (2007) and confirmed in numerical calculations, e.g., by Pons, Miralles & Geppert (2009). Nevertheless, this conclusion allows us to employ the local approximation and use our standard 1D cooling code for studying the main features of the heat transport from blob-like heaters. We employ this approach in the rest of this paper.

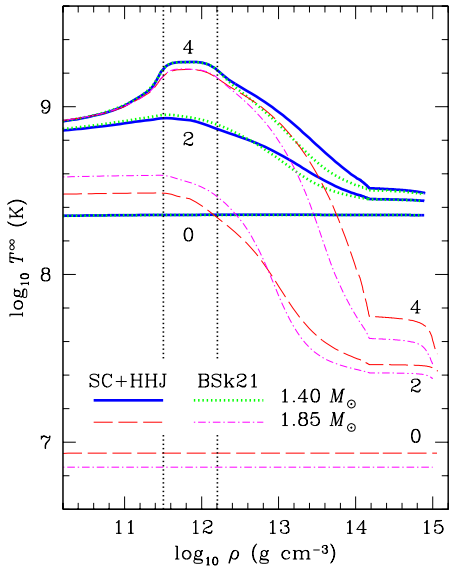

Figure 3. (Colour online) Temperature profiles $T^\infty(\rho)$ in the $1.4\,M_\odot$ (thick solid lines) and $1.85\,M_\odot$ (thin long-dashed lines) stars of age $t = 1$ kyr produced by a spherical heater (b) at two heat intensities (curves 2 and 4, Table 3) and without the heater (curves 0); ρ_1 and ρ_2 (vertical dotted lines) are the same as in Fig. 2. In addition to the curves calculated for the SC+HHJ model (solid and long-dashed lines), the curves for more realistic BSk21 EOS (dotted and dot-dashed lines, respectively) are plotted for comparison. See text for details.

4 CALCULATIONS WITH THE 1D CODE

4.1 Two regimes

Fig. 3 shows the redshifted temperature profiles $T^\infty(\rho) = T(\rho)\,\mathrm{e}^\Phi$ inside the 1.4 $M_\odot$ and 1.85 $M_\odot$ stars ("standard cooler" and "fast cooler" in Table 1) for the two EOS models: SC+HHJ and BSk21 (see Table 1). It is $T^\infty(\rho)$ [not $T(\rho)$] that is constant (independent of ρ) in isothermal regions of the star with account for General Relativity.

For each star and EOS we show three $T^\infty(\rho)$ profiles labelled 0, 2, and 4 according to Table 3. The profiles 0 correspond to no heating ($H_0 = 0$). The profiles 2 and 4 are for the heater with intensity $H_0 = 10^{19.5}$ and $10^{21.5}$ erg cm^{-3} s^{-1}, respectively, placed at $3.2 \times 10^{11} \leqslant \rho \leqslant 1.6 \times 10^{12}$ g cm^{-3} (case (b) in Table 2).

The curves 0 correspond to ordinary cooling neutron stars and decrease with the age t. Without heating, at $t =$ 1 kyr the bulk of the star is already thermally relaxed and T^∞ stays nearly constant over the stellar interior. In this case, the internal temperature of the fast cooler is about 30 times lower because of the enhanced neutrino cooling of the inner kernel of the star.

Other curves (for the heated stars) are different. The energy deposit in the crust destroys the thermally relaxed states and makes $T^\infty(\rho)$ variable within the star. The temperature profiles become mostly independent of t (as long as $t \ll \tau$), being supported by the heater. The stars stop to cool down and reach (quasi)stationary states (as plotted, e.g., in Figs. 2 and 3 of Paper I). The hottest place in the star is naturally the heater itself and its vicinity. The core and the surface are colder, so that the generated heat is carried away by thermal conduction to the surface and to the core. It is also radiated away by neutrinos from different layers of the star.

As long as the heat intensity is not too strong ($H_0 \lesssim 10^{20}$ erg cm^{-3} s^{-1}, curves 2), the temperature profiles in the fast cooler are noticeably lower than in the standard cooler. This is again because of the stronger neutrino emission in the core of the massive star; strong neutrino cooling in the core affects the heater even if it is quite close to the surface, e.g., in the vicinity of the neutron drip point. If the heating is stronger ($H_0 \gtrsim 10^{20}$ erg cm^{-3} s^{-1}; curves 4 in Fig. 3) the situation is different. The temperature around the heater ceases to depend on the neutrino emission in the core, which manifests thermal decoupling of the heater and the core, discussed below.

In each case, the results obtained for the two different EOSs (SC+HHJ and BSk21) are qualitatively similar but quantitatively different. The largest difference is observed in the core of the fast cooler at the highest heating level, where the BSk21 model predicts considerably lower temperature

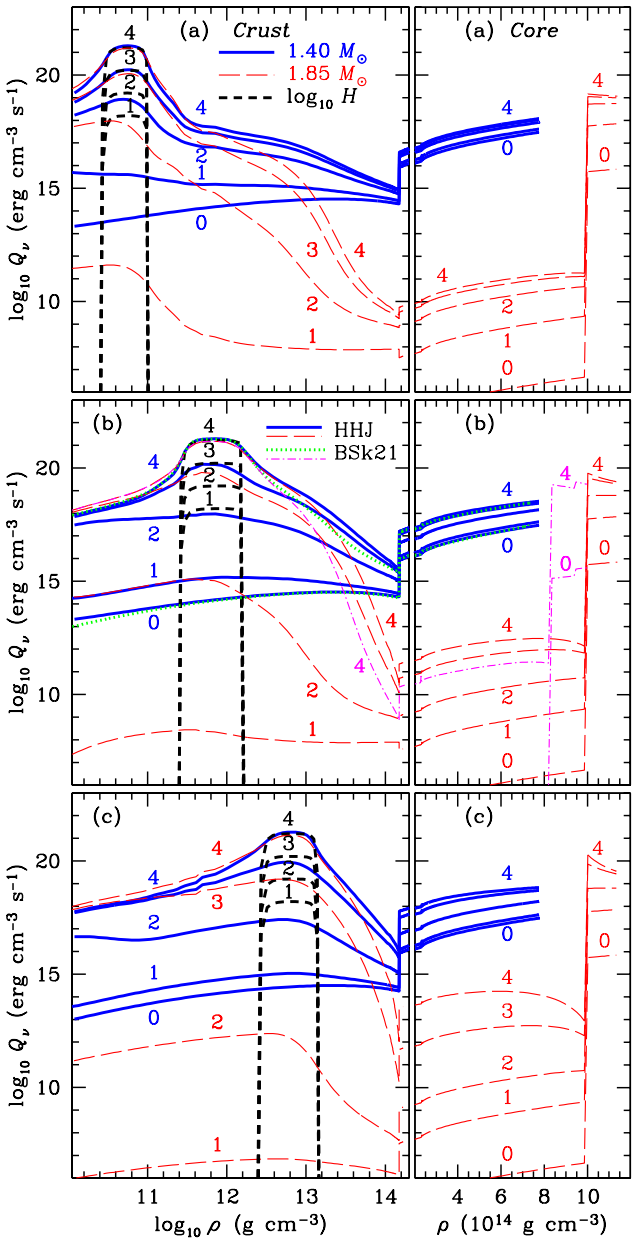

Figure 4. (Colour online) Logarithm of the neutrino emissivity (Q_ν) versus density in the $1.4\,M_\odot$ star (thick solid lines) and the $1.85\,M_\odot$ star (thin long-dashed lines) with the SC+HHJ EOS at $t = 1$ kyr for three positions of the heater (a), (b) and (c) and five heat intensities 0,. . . , 4 (Tables 2 and 3). The left section of every panel refers to the crust, with the density given in logarithmic scale; the right section refers to the core, where ρ is given in linear scale (in units of 10^{14} g cm^3). Short-dashed lines give logarithm of the heat intensity, $\log H$. Additional dotted and dot-dashed curves in the panels (b) show the results for $M = 1.4\,M_\odot$ and $1.85\,M_\odot$, respectively, calculated with the BSk21 EOS for the heating levels 0 and 4.

than the HHJ(0.1,0.7) model. This is because the Durca threshold is lower for the BSk21 EOS than for the HHJ EOS (see Table 1), which results in a more massive and accordingly more efficient fast-cooling kernel of the massive star.

Fig. 4 illustrates neutrino emission of the heated neutron stars. It shows logarithm of the neutrino emissivity Q_ν as a function of density throughout the $1.4\,M_\odot$ and $1.85\,M_\odot$ stars (thick solid and thin long-dashed lines, respectively). The three panels (a), (b) and (c) correspond to the three positions of the heater in the crust (Table 2). To visualize the details, the left section of each panel shows the crust with the density in logarithmic scale, while the right section shows the core with the density in linear scale. Visible jumps of the Q_ν curves at the crust-core interface (near the right vertical axis of the left panel) are due to the difference in neutrino emission mechanisms in the crust and the core. The central density of the $1.85\,M_\odot$ star is higher than that of the $1.4\,M_\odot$ star (Table 1). Accordingly, the Q_ν curves for the massive star are extended to higher ρ. The large jumps of the Q_ν curves at $\rho \sim 10^{15}$ g cm^{-3} for the $1.85\,M_\odot$ star are due to the onset of the Durca neutrino emission in the central kernel of the star.

Curves 0 correspond to ordinary cooling neutron stars. The corresponding neutrino emission depends on t. Since the fast cooler is much colder than the standard cooler (Fig. 3), its neutrino emission in the outer core is much weaker at densities before the Durca threshold, but becomes strongly enhanced in the inner kernel after the threshold.

Curves 1–4 correspond to neutron stars heated from the crust. Their neutrino emission is mainly "frozen" – independent of t (as long as $t \ll \tau$), being primarily supported by the newly generated heat.

For each position of the heater and each M we consider five levels of heat intensity H_0 from zero to $10^{21.5}$ erg cm^{-3} s^{-1} (curves 0,. . . ,4, Table 3). In each case we plot also logarithm of the heat power H. Fig. 4 allows one to judge how much of the input heat is transformed into neutrino emission and what is the distribution of neutrino sources. Note that in the preliminary publication (Kaminker et al. 2012) similar curves $Q_\nu(\rho)$ in Fig. 1(c) for $\log H_0$=18.5 and 19.5 were plotted inaccurately.

In the middle panels (b) of Fig. 4 we additionally plot $Q_\nu(\rho)$ calculated for the BSk21 EOS model in the cases of no heating and maximal heating. For the standard cooling ($M = 1.4\,M_\odot$), the profiles $Q_\nu(\rho)$ for the two EOSs are almost indistinguishable without heating and remain very close to each other at the highest heating rate. For the fast cooling ($M = 1.85\,M_\odot$), differences are more significant. First, the jump at the Durca threshold is shifted to lower density according to Table 1 (see the right panel (b)). Second, the neutrino emissivity becomes much lower at $\rho \gg 10^{13}$ g cm^{-3}, which is directly related to the lower T^∞ in Fig. 3 due to the lower Durca threshold, as explained above.

An analysis of Figs. 3 and 4 (and other figures presented below, as well as many other numerical results not shown here) indicates the existence of two drastically different regimes of energy outflow from the heater. These regimes are also summarized in Table 4.

(i) *The conduction outflow regime* occurs at not too high heat rates ($H_0 \lesssim 10^{20}$ erg cm^{-3} s^{-1}, curves 1 and 2 in Fig. 4) which produce not too high temperatures $T_\mathrm{h} \lesssim 10^9$ K within the heater. In these cases, $H \gg Q_\nu$ within the heater. The heater's energy is mainly carried away by thermal conduction. A larger fraction of this energy sinks to the core and is emitted from there by neutrinos. The thermal state of the crust in the heater and its vicinity, as

Table 4. Two regimes of heat transport from the heater

Regime	H_0 erg cm^{-3} s^{-1}	T_h K	Thermal emission	Coupling to core
(i) Conduction outflow	$\lesssim 10^{20}$	$\lesssim 10^9$	depend on H_0	yes
(ii) Neutrino outflow	$\gtrsim 10^{20}$	$\gtrsim 10^9$	saturated	no

well as the thermal surface emission, are very sensitive to the neutrino cooling in the core (modified or direct Urca): there is *a strong thermal coupling between the surface and the core*.

(ii) *The neutrino outflow regime* occurs at rather high heat rates ($H_0 \gtrsim 10^{20}$ erg cm^{-3} s^{-1}, curves 3 and 4 in Fig. 4), i.e. at high temperatures $T_\mathrm{h} \gtrsim 10^9$ K within the heater. The heat power H within the heater is close to Q_ν, which means that the heat is mainly radiated away by neutrinos *just in the heater*. A smaller fraction is carried away by thermal conduction to the core, and only a tiny fraction of the heat is conducted to the surface and radiated away as thermal emission. The thermal states of the crust around the heater, as well as thermal radiation from the surface, become insensitive to the neutrino cooling in the core implying that *the core is thermally decoupled from the crust*.

It is remarkable that the characteristic heat intensity H_0 and heater's temperature T_h, that separate regimes (i) and (ii), are almost independent of the heater's position in the crust. Note, however, that according to Paper II, T_h exceeds the characteristic value $\sim 10^9$ K (at the same $H_0 \gtrsim 10^{20}$ erg cm^{-3} s^{-1}) if we shift the heater closer to the surface (when $\rho_1 \lesssim 10^{10}$ g cm^{-3}), but here we do not analyze such shallow heaters. Note also that when the heater is hot enough, the convective heat transport may be initiated in the heater or its vicinity, which we neglect for simplicity.

Because of different heat outflow regimes, one and the same neutron star can show very different behavior if the heat power varies within large limits. Let us remark also that our consideration of thermal coupling/decoupling between the surface and the core described above is strictly valid for spherical heaters. When the heater looks like a blob and operates in the neutrino cooling regime, the hot spot on the surface and the heater itself are decoupled from the core. However, the surface layers outside the hot spot can be thermally coupled to the core.

Fig. 5 shows the density dependence of redshifted thermal heat-conduction flux through spherical surfaces in the star (in units of solar luminosity $L_\odot$) for the heater (b) (Table 2) with four heat intensities H_0 (levels 1–4, Table 3). The thick solid lines are for the $1.4\,M_\odot$ star, and the thin dashed lines are for the $1.85\,M_\odot$ star. The flux is positive when the heat flows to the surface and negative when the heat is conducted to the star's center. The curves are calculated at $t = 1$ kyr, but they are virtually independent of t. The higher H_0, the larger the heat flux. The largest fluxes occur at the heater's boundaries ρ_1 and ρ_2; in these places the fluxes are sensitive to the shape of the heat power distribution $H(\rho)$.

Any flux vanishes at a certain *zero-flux surface* between the heater's boundaries. Above the zero-flux surface the heat flows outwards; below this surface it flows to the core. In the heat outflow regime the zero-flux surface is closer to the outer heater's boundary, ρ_1. In the neutrino outflow regime it shifts to the center of the heater, where the heat intensity is maximal. For all heat intensities, maximum positive fluxes are significantly lower than maximum negative ones. Accordingly, the amount of the heat which flows to the star's surface is much smaller than that which flows to the core. In the outer core of the $1.85\,M_\odot$ star the heat conduction flux is almost constant because of low neutrino emission (Fig. 4); in the inner kernel this flux rapidly decreases, because the Durca process produces strong neutrino cooling there.

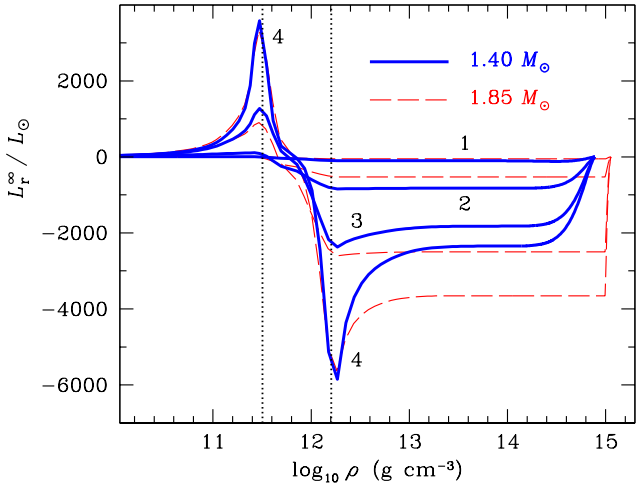

Figure 5. (Color online) Redshifted heat flux $L^\infty(\rho)/L_\odot$ through spherical surfaces in the $1.4\,M_\odot$ star (thick solid lines) and $1.85\,M_\odot$ star (thin dashed lines) with the SC+HHJ EOS at $t = 1$ kyr versus ρ; the flux is directed outward (if positive) or inward (if negative). The flux is produced by spherical heater (b) (whose position is marked by dotted lines) at four heat intensities 1–4; in all the cases the fluxes are relatively small at $\rho = \rho_\mathrm{b} = 10^{10}$ g cm^{-3}.

4.2 How to warm up the surface

The main observational manifestation of the heater is the thermal emission from the neutron star surface. Here we analyze the ability of the heater to warm up the surface. The main obstacle for warming up the surface is clear: the heat is mostly conducted inside the star and radiated away by neutrinos.

Fig. 6 shows the excess surface heat flux ΔF_L from the $1.4\,M_\odot$ and $1.85\,M_\odot$ stars with the SC+HHJ EOS (thick solid and thin dashed lines, respectively) and heaters of different intensities H_0 placed in four different regions (a)–(d) of the crust (Table 2). Recall (Sect. 2) that we have chosen the widths of the heaters (a)–(d) in such a way that they produce the same heat power W^∞ for the same heat intensity H_0. In Fig. 6 we vary H_0 in a wide range. The upper line of each type (solid or dashed) shows the flux $F_W = W/(4\pi R^2)$ (not redshifted for a distant observer) as a function of H_0. It is determined by the total non-redshifted heat power $W \approx W^\infty/(1 - r_g/R)$, where $r_g = 2GM/c^2$ is the Schwarzschild radius of the star, and W^∞ is defined by Eq. (3). Other lines show the excess thermal flux ΔF_L which

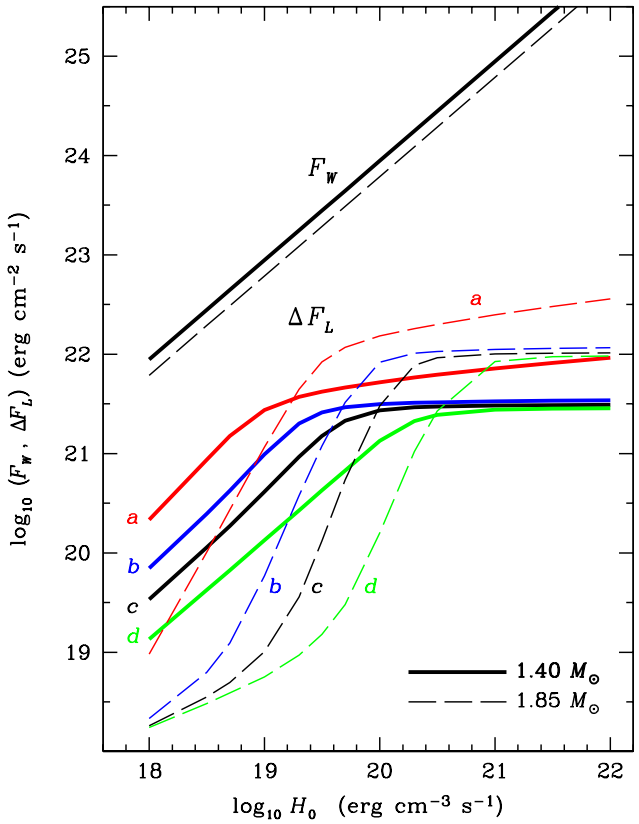

Figure 6. (Colour online) Generated heat flux F_W and excess surface flux ΔF_L for the standard cooler (solid lines) and fast cooler (dashed lines) as functions of heat intensity H_0 for different heater models. The upper straight lines of each type (solid or dashed) show the total heat flux $F_W = W/(4\pi R^2)$ at $t = 1$ kyr (in a local reference frame) generated by the heater. The other lines are excess heat fluxes ΔF_L through the stellar surface from the heater of the same total power W placed in four regions (a)–(d). The SC+HHJ EOS is used. See text for details.

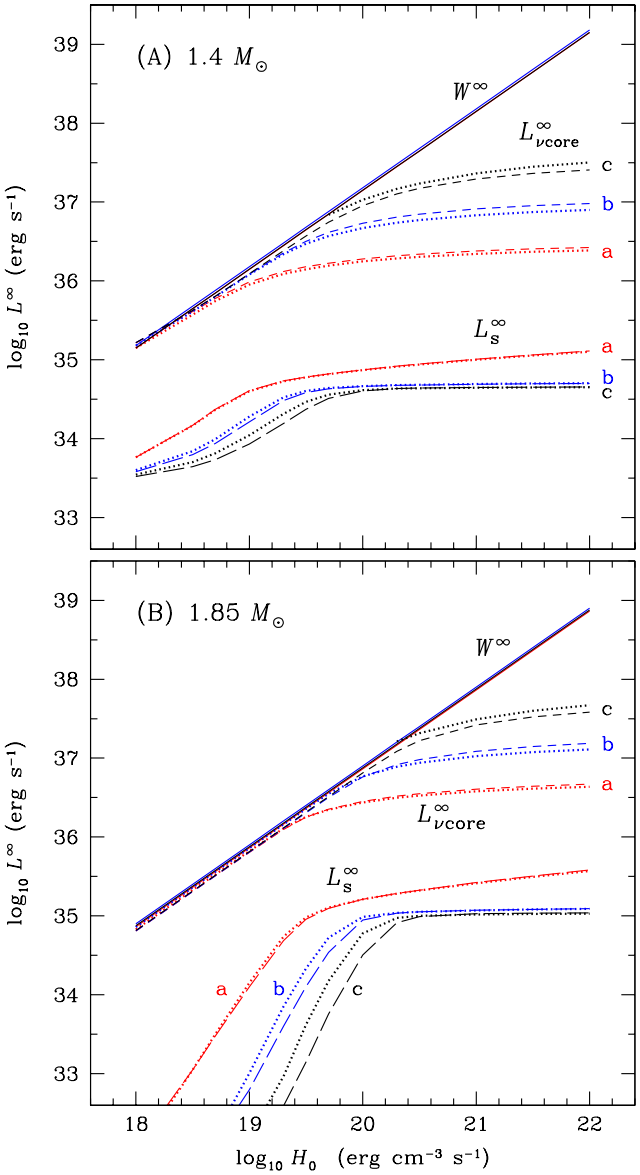

Figure 7. (Colour online) Total redshifted heat power W^∞ (thick solid lines), the main part of integrated redshifted neutrino luminosity of the core $L^\infty_{\nu\rm core}$ (short-dashed lines), provided by the crust-to-core heat flux (see text), and surface thermal luminosities $L^\infty_{\rm s}$ (long-dashed lines) versus $\log H_0$ for the $1.4\,M_\odot$ star [panel (A)] and the $1.85\,M_\odot$ star [panel (B)] at the three heater's positions (a)–(c), for the SC+HHJ EOS model. The dotted lines that are close to the dashed ones show the corresponding luminosities calculated with the alternative model BSk21.

reaches the surface from the heaters (a)–(d). The $\Delta F_L/F_W$ ratio can be called the *efficiency of the heater* to warm up the surface (with $\Delta F_L/F_W = 1$ if all the heater's energy could reach the surface).

For example, the heater (b) with $H_0 = 3 \times 10^{19}$ erg cm^{-3} s^{-1} in the $1.4\,M_\odot$ star would produce $F_W \approx 2.8 \times 10^{23}$ and $\Delta F_L \approx 2.6 \times 10^{21}$ erg s^{-1} cm^{-2}, with $\Delta F_L/F_W \approx 10^{-2}$. The same heater in the $1.85\,M_\odot$ star would generate $F_W \approx 1.9 \times 10^{23}$ and $\Delta F_L \approx 1.2 \times 10^{21}$ erg s^{-1} cm^{-2}, with $\Delta F_L/F_W \approx 6 \times 10^{-3}$. Recall once more that such quasi-stationary thermal states of these stars are determined by the heater. Stars without heater would cool down. For instance, in the age interval from $t = 1$ to 10 kyr, the thermal flux F_{L0} of the ordinary cooling $1.4\,M_\odot$ star would decrease from 2.1×10^{20} to 8.4×10^{19} erg s^{-1} cm^{-2}, while for the $1.85\,M_\odot$ star it would decrease from 7.5×10^{17} to 2.0×10^{17} erg s^{-1} cm^{-2}.

Note that each group of curves in Fig. 6, solid or dashed, which represent the excess surface flux ΔF_L as functions of H_0, would look exactly the same as functions of the total generated flux F_W, because F_W is a linear function of H_0 by construction. In this way it is easy to see, how much of the generated heat is radiated through the surface.

Fig. 7 displays redshifted surface thermal luminosities L^∞_s (long-dashed lines) emitted by the $1.4\,M_\odot$ and $1.85\,M_\odot$ stars [panels (A) and (B), respectively] as functions of H_0, calculated for the SC+HHJ EOS. The heaters are placed in three regions (a)–(c). In every case, a nearby dotted line shows an analogous dependence for the BSk21 EOS. We plot also the total redshifted heat power W^∞ (solid lines), and the dominant part of the integrated redshifted neutrino luminosity from the star's core $L^\infty_{\nu\rm core}$ (short-dashed lines) equal to the total heat flux that passes from the crust to the

core. These curves illustrate the contribution in the heat balance of the neutrino emission from the core.

Let us outline the main features of the conduction outflow regime (Table 4). In this regime the extra thermal flux ΔF_L and the surface luminosity L_s^∞ increase with increasing H_0. This increase is sensitive to the physics of the stellar core because of the thermal coupling between the core and the surface. For the standard neutrino emission level in the core (the modified Urca process) one approximately has $\Delta F_L \propto H_0$ (Fig. 6). One can show that this occurs for a warm heater, where the thermal conductivity weakly depends on temperature (e.g., Gnedin et al. 2001). For the enhanced neutrino emission (the Durca process) at $H_0 \lesssim 10^{19}$ erg cm^{-3} s^{-1} the star is colder and ΔF_L is lower than for the standard process. However, ΔF_L increases faster at $H_0 \gtrsim 10^{19}$ erg cm^{-3} s^{-1} and overcomes the standard values ΔF_L at higher H_0.

At lower H_0 in a massive cold star, the thermal conductivity increases with lowering T and destroys the relation $\Delta F_L \propto H_0$. Note that we use the standard electron thermal conductivity in the crust, neglecting possible effects of ion impurities (e.g., Potekhin et al. 1999) and effects of distortion of electron wave functions due to interaction with the Coulomb lattice (Chugunov 2012). Both effects can strongly slow down the increase of the conductivity mention above and affect thereby the relation between ΔF_L and H_0 at $H_0 \ll 10^{19}$ erg cm^{-3} s^{-1} in massive stars.

In the conduction outflow regime L_s^∞ increases with W^∞. The heater is divided into outer and inner parts, and the heat is conducted to the surface from the outer part (Fig. 5).

In the intermediate regime, at $H_0 \sim 10^{20}$ erg cm^{-3} s^{-1}, when the conduction outflow regime transforms to the neutrino outflow regime, the flux ΔF_L becomes nearly independent of the neutrino emission in the core, but is mainly controlled by neutrino emission in the crust. This signifies the onset of thermal decoupling between the surface and the core.

Finally we outline the neutrino outflow regime. In this case the flux ΔF_L and the luminosity L_s^∞ saturate and become almost independent of H_0 (and of the physics of the core), except for the case (a) where the heat conduction to the surface is more competitive with the neutrino cooling. We expect that moving the heater even closer to the surface would increase the surface thermal flux. However, for crustal heaters located in the layers considered here, the generated surface thermal flux weakly depends on the heat power and on the internal structure of the star, while the efficiency of surface photon emission $\Delta F_L/F_W$ decreases with growing H_0. The heater can generate enormous amount of energy but it will be mostly radiated by neutrinos and will not increase the surface flux. This limiting surface flux comes from a thin outer layer of the heater. Making the heater wider by extending it deeper within the crust will not change the photon surface emission.

Therefore, there exist *the maximum flux* $\Delta F_L^{\max}$ that can emerge from a steady state heater in the neutrino outflow regime. This maximum flux is almost the same for heaters (b)–(d) located deeper in the crust. According to Fig. 6, $\Delta F_L^{\max} \approx 3 \times 10^{21}$ and $\Delta F_L^{\max} \approx 10^{22}$ erg cm^{-2} s^{-1} for the $1.4\,M_\odot$ and $1.85\,M_\odot$ stars, respectively. It is smaller than the Eddington flux (the maximum steady radiation flux emergent through the neutron star surface) by a factor of $\sim 10^{-4} - 10^{-3}$. The existence of such a maximum radiation surface flux limited by neutrino emission has been pointed out for magnetars (Papers I and II; Pons & Rea 2012), but it evidently exists for all neutron stars. In contrast to the papers mentioned above we calculate it here assuming no anisotropy of heat transport in the neutron star envelopes, particularly, in heat blanketing layers. For the heater (a), which is closer to the surface, $\Delta F_L^{\max}$ is higher. We expect that moving the heater even closer to the surface would further increase $\Delta F_L^{\max}$ making it closer to the Eddington limit. These results imply that when a neutron star radiates steadily at nearly Eddington luminosity, its radiation cannot be powered by internal sources.

To summarize, the most efficient heater would be intermediate between the conduction and neutrino outflow regimes ($H_0 \sim 10^{20}$ erg cm^{-3} s^{-1}) and placed in the outer crust. It would be uneconomical for the energy budget to place the heater in the deep inner crust or to generate too much heat ($H_0 \gg 10^{20}$ erg cm^{-3} s^{-1}). This conclusion, already known for magnetars, remains valid for all neutron stars.

In the neutrino outflow regime the efficiency of the heater in the $1.85\,M_\odot$ star is somewhat higher than in the $1.4\,M_\odot$ star. This result seems counter-intuitive because the massive star undergoes a very strong neutrino cooling. However, it is true, because the more massive star has a thinner crust, which facilitates heat conduction to the surface.

The results of this section can be affected by strong magnetic fields $B \gtrsim 10^{13}$ G and by chemical composition of the heat blanketing envelope (as discussed, e.g., in Papers I and II). The strongest effects are expected to occur for most shallow heater's locations.

5 DISCUSSION

In this section we outline the most important possible manifestations of the internal heaters in neutron stars.

5.1 Young cooling neutron stars

Numerous simulations of young cooling neutron stars (e.g., Lattimer et al. 1994; Yakovlev et al. 2001) demonstrate the existence of quasi-stationary thermal flux emergent from neutron star interiors. For instance, Figs. 25 and 26 of Yakovlev et al. (2001) show cooling curves of non-superfluid neutron stars of different masses with two model EOSs in the core. They display the cooling "as observed from outside." There is a visible surface temperature drop at $t \sim 10 - 10^2$ yr (depending on neutron star models and microphysics input). It manifests the end of the initial thermal relaxation inside cooling neutron stars. Snapshots of the redshifted temperature profiles $T^\infty(\rho)$ (of "inside cooling") at different moments of time t for two neutron stars of different masses are shown in Figs. 27 and 28 of Yakovlev et al. (2001). Figures 25–28 of that paper clearly demonstrate the effects of temperature variations in a cooling neutron star on its thermal photon emission.

Before the thermal relaxation ends, a star is strongly non-isothermal inside. The crust is hotter than the core because of lower neutrino emission in the crust. The relaxation

consists mainly in the core-crust equilibration. It is accompanied by violent processes of non-uniform neutrino cooling and heat conduction; the interior of the star is highly non-isothermal, but the surface temperature T_s in the period from ~ 0.1 yr till the relaxation end stays wonderfully constant, as if the star were thermally equilibrated, which is definitely not the case!

Such quasistationary states of young cooling non-relaxed neutron stars appear because the temperature in some parts of the crust (Figs. 27 and 28 of Yakovlev et al. 2001) exceeds 10^9 K. This triggers the neutrino outflow regime and the associated thermal decoupling. Then the quasistationary thermal surface luminosity reaches the maximum luminosity that the star can have (see Sect. 4). Hot layers of the crust perform as powerful effective heaters. This explains the results of numerous cooling simulations of young neutron stars. Let us remark that the surface luminosity of very young stars ($t \lesssim 0.1$ yr) is above the quasistationary level and noticeably decreases with time. This is because the very young neutron stars are far from the steady state discussed in Sect. 4.

Note that some cooling simulations (e.g., Blaschke et al. 2004 and subsequent publications based on similar microphysics) predict much stronger thermal emission from surfaces of young neutron stars. These results are obtained with non-standard physics of outer neutron-star layers.

5.2 Neutron stars in soft X-ray transients

Internal heat sources operate also in transiently accreting neutron stars in low-mass X-ray binaries (LMXBs; see, e.g., Wijnands, Degenaar & Page 2013; Turlione, Aguilera & Pons 2013 and references therein). These objects can be in active or quiescent states. In the active states, neutron stars accrete matter from their low-mass companions through accretion disks. The accretion strongly heats the neutron star surface and triggers X-ray bursts in the surface layers. Then the neutron star is observed as a bright X-ray source. Active states are followed by quiescent states when the accretion is quenched. Then X-ray luminosity decreases, but the neutron star still shows noticeable thermal X-ray emission indicating that it remains warm inside.

Quiescent thermal emission of transiently accreting neutron stars in LMXBs is currently explained (Brown et al. 1998) by the deep crustal heating of these stars (Haensel & Zdunik 1990, 2008). This heating operates over the active states in the crustal matter compressed by newly accreted material. The compression induces nuclear transformations (absorption/emission of neutrons; electron captures; pycnonuclear reactions) with release of $\sim$ 1–2 MeV per accreted nucleon, predominantly, in the inner crust.

Observations combined with theoretical models indicate (e.g., Wijnands et al. 2013; Turlione et al. 2013) that the deep crustal heating is insufficiently strong to endure the thermal decoupling. All the sources remain in the conduction outflow regime but behave in different ways.

First, most of the sources perform as quasi-stationary ones (e.g., Aql X-1), where the heater is not very strong or operates for not too long, so that it does not violate internal isothermality. The heater warms up the star during the active states, and the heating is followed by the cooling in the quiescent states. Such stars are thermally inertial; heat gains and losses are thought to be balanced over a few accretion cycles; the star reaches a quasi-stationary state determined by crustal heating rate (i.e., by the mass accretion rate) averaged over $t \sim$ 100–1000 yr.

Second, some sources (such as MXB 1659–298, KS 1731–260, EXO 0748–676, XTE J1701–462, IGR J17480–2446, MAXI J0556–332; see, e.g, Degenaar et al. 2013a,b, and references therein) can be essentially nonstationary. In these cases the heater is strong or operates for a sufficiently long time to overheat the crust and violate the thermal balance of the crust with the core. After the accretion stops, the crust starts to thermally equilibrate with the core, which is manifested by a surface temperature fall in the quiescent state over a few months–years. It is actually the crust cooling observed in real time. In contrast to the thermal relaxation in young neutron stars (Sect. 5.1), this relaxation proceeds in the conduction outflow regime and does not contain the stage of internal thermal decoupling.

5.3 Magnetars and high-B pulsars

Our results can help to interpret observations of soft gamma repeaters (SGRs) and anomalous X-ray pulsars (AXPs), which are thought to be magnetars, viz. neutron stars with superstrong magnetic fields $B \gtrsim 10^{14}$ G (e.g., Mereghetti 2008; Rea & Esposito 2011; Mereghetti 2013; Olausen & Kaspi 2014). The results can aslo be useful for understanding the relations of the above sources to rotation powered high-B pulsars (e.g., Livingstone et al. 2011; Olausen et al. 2013). Let us outline the physics of these objects, which is possibly affected by internal heating.

SGRs and AXPs demonstrate slow rotation and large spindown rates indicating they have very strong magnetic fields. There is increasing evidence for the absence of any real difference between AXPs and SGRs (e.g., Gavriil, Kaspi, & Woods 2002; Mereghetti 2013). SGRs/AXPs exhibit large persistent thermal and non-thermal high-energy emission, X-ray and gamma-ray bursts and flares (losing more energy than their magnetic braking). This indicates wild processes of energy release in their interiors and/or magnetospheres.

Moreover, AXPs/SGRs seem related to high-B pulsars (e.g., Kaspi 2010; Mereghetti 2013; Rea 2013). The high-B pulsars show persistent thermal emission which is intermediate between magnetars and standard radio pulsars, and, at least for one case (PSR J1846–0258, Gavriil et al. 2008), they demonstrate magnetar-like outbursts. A high-B pulsar can exhibit X-ray bursts and then return to its initial state (e.g., Livingstone et al. 2011).

SGR/AXP-like activity is revealed even by some X-ray sources, whose spin-down indicate lower fields $B \ll 10^{14}$ G; this may be a late manifestation of magnetar activity which is expected to decay with age (e.g., Turolla & Esposito 2013; Rea 2013; Zhou et al. 2014; Rea et al. 2014 and references therein).

It seems that these features can be understood assuming that magnetized neutron stars possess persistent or variable internal heaters. When the heaters are on, neutron stars can behave as SGRs/AXPs, but when the heaters are off or weak, they behave as pulsars. Of course, this internal

activity can be closely related to the magnetospheric one (e.g. Beloborodov 2013).

Because energy reservoirs for the heaters are limited, the heaters should be economical (located not too deep in the crust and be not too strong, Sect. 4). Such sources can produce thermal decoupling between the neutron-star surface and the interior. Note that the heater's efficiency can be higher in a more massive star (with thinner crust), in a star with stronger magnetic field ($B \gtrsim 10^{13}$ G) or in a star with heat blanketing envelope composed of light elements (Papers I and II).

The heater's model may be like this. If the heater is located in the outer crust or near it, typical length-scales of pressure and density variations are small and the electric conductivity is low (especially if the heater is hot). Then the heater may be located in a special region, where nonlinear MHD instabilities (triggered by crustal breaking or magnetospheric activity) could take place. Here the Ohmic decay of electric currents can be strongly enhanced and produce the required amount of heat (e.g., Kaminker et al. 2012, Viganò et al. 2013). The heaters may be variable over months-years (appear, move, or almost disappear), which can regulate long-term variability of magnetar activity. Our results may help to develop a selfconsistent theory of quasi-stationary states. Another serious problem is to explain magnetar outbursts, their origin and relaxation; there is a variety of ideas, e.g., Perna & Pons 2011, Pons & Perna 2011, Levin & Lyutikov 2012, Viganò et al. 2013, and references therein.

An important problem is the energy delivery to the magnetic heater. Magnetars lose too much energy, which cannot be stored within one heater's region. This energy can be accumulated in the internal magnetic field of the star and then transported to the heater (e.g., Viganò et al. 2013). Evidently, the theory of magnetar structure and evolution should be further elaborated.

5.4 Neutron star mergers

Merging neutron stars attract wide attention (e.g., Faber & Rasio 2012), mainly because they are perspective objects to be detected by the new generation of gravitational observatories (like advanced LIGO). Gravitational signals from binary neutron star mergers are thought to carry important information on the internal structure of neutron stars.

Before neutron stars merge, they are likely heated by hydrodynamical motions due to tidal interactions and associated phenomena. One can treat this heating as produced by internal heaters, so that the results of Sect. 4 can apply, at least qualitatively. The main outcome is that after the internal temperature becomes sufficiently high in certain layers of merging neutron stars, the neutrino outflow regime starts to operate and govern the thermal evolution of these layers. The thermal energy in these layers will be efficiently carried away by neutrinos. A disregard of neutrino emission in numerical simulations may lead to inadequate physical picture of merging neutron stars.

6 CONCLUSIONS

We have studied the thermal surface radiation from neutron stars with steady internal heaters. We have used our new 2D code to consider blob-like heaters and our standard 1D code to consider heaters located in spherically symmetric layers. We have varied the sizes of the heaters, as well as their power and position within the crust. We have used neutron star models of two masses, $1.4\,M_\odot$ and $1.85\,M_\odot$. The $1.4\,M_\odot$ star has the standard neutrino emission from the core via the modified Urca process, while the $1.85\,M_\odot$ star has the fast neutrino emission via the Durca process. We have used two EOSs, SC+HHJ and BSk21. The first of them is based on a simple energy-density function and serves for our calculations in most cases. The second one is more elaborated and more realistic; it serves to examine the sensitivity of the results to variations of EOSs.

Our main aim was to investigate how much energy of a heater can be emitted through the surface as thermal radiation, and which information on the heater and internal structure of neutron stars can be inferred from observations of this radiation.

Our main conclusions are the following.

(i) Comparison of 1D and 2D calculations reveals that generated heat has no tendency to spread along the star's surface. The heat mainly diffuses to the interior of the star and is carried away by neutrinos from there, but a small fraction diffuses outwards and is emitted as thermal surface radiation. The heater creates a hot spot, which is just the projection of the heater onto the surface. Therefore, heat propagation (excluding some special cases; Sect. 3) can be approximately studied with the local 1D approximation.

(ii) The heater can operate in the two regimes. If its power is not very strong, so that the temperature in the heater $T_\mathrm{h} \lesssim 10^9$ K ($H_0 \lesssim 10^{20}$ erg cm^{-3} s^{-1}), then thermal transport within the heater is mainly conductive. In this case the surface emission can be greatly reduced by the enhanced neutrino emission in the stellar core of a massive star. On the other hand, it can intensified by the growth of the heater's power.

(iii) If the heater is more powerful ($T_\mathrm{h} \gtrsim 10^9$ K; $H_0 \gtrsim 10^{20}$ erg cm^{-3} s^{-1}), its energy is mainly carried away by neutrinos. The surface thermal radiation becomes independent of the heater's power and of the physics of the core; it is the maximum thermal radiation which can be carried away from the heater of given geometry by conduction and emitted through the stellar surface. In this regime, the surface becomes thermally decoupled from the interior and even strong variations of heater's power cannot significantly change the surface emission.

(iv) The most economical heater, which transports to the surface the maximum fraction of the released energy, should be placed in the outer crust and be moderately strong ($H_0 \sim 10^{20}$ erg cm^{-3} s^{-1}) to avoid non-economical neutrino cooling. Its efficiency can be still higher in a more massive neutron star (with thinner crust), in the presence of a superstrong magnetic field or in the case where the blanketing envelope consists of light elements.

Some of these conclusions were previously drawn for strongly magnetized neutron stars (e.g., Papers I and II). Now we have shown that they are pertinent to all neutron

stars, including non-magnetized ones. These conclusions are robust, they do not depend on the concrete EOS we use.

We have outlined (Sect. 5) possible applications of the above results to young neutron stars, neutron stars in soft X-ray transients, to magnetars and high-B pulsars, as well as to merging neutron stars. Other applications include, for instance, heating due to viscous friction in the presence of differential rotation (e.g., Chirenti et al. 2013), slow chemical equilibration of the star in the course of its evolution (Petrovich & Reisenegger 2010), thermal evolution of pulsars after glitches.

It is important to account for the neutrino outflow regime in hot neutron stars with strong heaters. Such a heater drastically affects the heat transport mechanisms and produces thermal decoupling of the heater from deeper regions of the star. We argue that this regime can be realized in young cooling neutron stars before the end of internal thermal relaxation, in magnetars, and in merging neutron stars. In this paper we have studied steady state heaters. It would be interesting to extend the analysis to variable heaters.

ACKNOWLEDGMENTS

The authors are grateful to anonymous referee for careful reading of the manuscript and useful comments. This work has been partly supported by the RFBR (grant No. 14-02-00868-a) and by the State Program "Leading Scientific Schools of RF" (grant NSh 294.2014.2).

References

Aguilera D. N., Pons J. A., Miralles J. A., 2008, A&A 486, 255
Akmal A., Pandharipande V. R., Ravenhall D. G., 1998, Phys. Rev. C 58, 1804
Antoniadis J. et al., 2013, Science 340, 448
Baiko D. A., Potekhin A. Y., Yakovlev D. G., 2001, Phys. Rev. E 64, 057402
Beloborodov A. M., 2013, ApJ 762, 13
Blaschke D., Grigorian H., Voskresensky D. N., 2004, A&A 424, 979
Brown E. F., Bildsten L., Rutledge R. E., 1998, ApJ 504, L95
Chirenti C., Skakala J., Yoshida S. 2013, Phys. Rev. D 87, 044043
Chugunov A. I., 2012, Astron. Lett. 38, 25
Degenaar N. et al., 2013a, ApJ 775, 48
Degenaar N., Wijnands R., Miller J. M., 2013b, ApJ 767, L31
Demorest P. B., Pennucci T., Ransom S. M., Roberts M. S. E., Hessels J. W. T., 2010, Nature 467, 1081
Espinoza C. M., Lyne A. G., Stappers B. W., Kramer M., 2011, MNRAS 414, 1679
Faber J. A., Rasio F. A., 2012, Living Reviews in Relativity 15, no. 8
Fortin M., Grill F., Margueron J., Page D., Sandulescu N., 2010, Phys. Rev. C 82, 065804
Gavriil F. P, Kaspi V. M, Woods P. M., 2002, Nature 419, 142
Gavriil F. P., Gonzalez M. E., Gotthelf E. V., Kaspi V. M., Livingstone M. A., Woods P. M., 2008, Science 319, 1802
Gnedin O. Y., Yakovlev D. G., Potekhin A. Y., 2001, MNRAS 324, 725
Goriely S., Chamel N., Pearson J. M., 2010, Phys. Rev. C 82, 035804
Gudmundsson E.H., Pethick C.J., Epstein R. I., 1983, ApJ 272, 286
Gusakov M. E., Kaminker A. D., Yakovlev D. G., Gnedin O. Y., 2005, MNRAS 363, 555
Haensel P., Zdunik J. L., 1990, A&A 227, 431
Haensel P., Zdunik J. L. 2008, A&A 480, 459
Haensel P., Potekhin A. Y., Yakovlev D. G., 2007, Neutron Stars 1. Equation of State and Structure. Springer, New York
Heiselberg H., Hjorth-Jensen M., 1999, ApJ 525, L45 (HHJ)
Kaminker A. D., Yakovlev D. G., Potekhin A. Y., Shibazaki N., Shternin P. S., Gnedin O. Y., 2006, MNRAS 371, 477 (Paper I)
Kaminker A. D., Potekhin A. Y., Yakovlev D. G., Chabrier G., 2009, MNRAS 395, 2257 (Paper II)
Kaminker A. D., Kaurov A. A., Potekhin A. Y., Yakovlev D. G., 2012, ASP Conf. Ser. 466, 237
Kaspi V., 2010, Publ. Nat. Acad. Sci. USA 107, 7147
Lattimer J. M., Pethick C. J., Prakash M., Haensel P., 1991, Phys. Rev. Lett. 66, 2701
Lattimer J. M., van Riper K. A., Prakash M., Prakash M., 1994, ApJ 425, 802
Levin Y., Lyutikov M., 2012, MNRAS, 427, 1574
Li Z. H., Schulze H.-J., 2008, Phys. Rev. C 78, 028801
Livingstone M. A., Ng C.-Y., Kaspi V. M., Gavriil F. P., Gotthelf E. V., 2011, ApJ 730, 66
Mereghetti S., 2008, A&ARv 15, 225
Mereghetti S., 2013, Braz. J. Phys. 43, 35
Olausen S. A., Kaspi V. M., 2014, ApJS 212, 6
Olausen S. A. et al., 2013, ApJ 764, 1
Page D., Geppert U., Weber F., 2006, Nucl. Phys. A 777, 497
Pearson J. M., Chamel N., Goriely S., Ducoin C., 2012, Phys. Rev. C 85, 065803
Perna R., Pons J. A., 2011, ApJ, 727, L51
Petrovich C., Reisenegger A. 2010, A&A 521, A77
Pons J. A., Perna R., 2011, ApJ, 741, 123
Pons J. A., Rea N., 2012, ApJ, 750, L6
Pons J. A., Miralles J. A., Geppert U., 2009, A&A 496, 207
Potekhin A. Y., Chabrier G., Yakovlev D. G., 1997, A&A 323, 415
Potekhin A. Y., Baiko D. A., Haensel P., Yakovlev D. G., 1999, A&A 346, 345
Potekhin A. Y., Yakovlev D. G., Chabrier G., Gnedin O. Y., 2003, ApJ 594, 404
Potekhin A.Y., Chabrier G., Yakovlev D.G., 2007, Ap&SS 308, 353; corrected version: arXiv:astro-ph/0611014v3
Potekhin A. Y., Fantina A. F., Chamel N., Pearson J. M., Goriely S., 2013, A&A 560, A48
Rea N., 2013, in Neutron Stars and Pulsars: Challenges and Opportunities after 80 years (Proc. IAU Symp. 291), J. van Leeuwen, ed., Cambridge University Press, Cambridge, p. 11
Rea N., Esposito P. 2011, in High-Energy Emission from Pulsars and Their Systems, D. F. Torres & N. Rea, eds.,

Springer, Berlin, p. 247
Rea N., Viganò D., Israel G. L., Pons J. A., Torres D. F., 2014, ApJ 781, L17
Rüster S. B., Hempel M., Schaffner-Bielich J., 2006, Phys. Rev. C 73, 035804
Turlione A., Aguilera D. N., Pons J. A., 2013, arXiv:1309.3909
Turolla R., Esposito P., 2013, Int. J. Mod. Phys. D 22, 1330024
Viganò D., Rea N., Pons J. A., Perna R., Aguilera D. N., Miralles J. A., 2013, MNRAS 434, 123
Wijnands R., Degenaar N., Page D., 2013, MNRAS 432, 2366
Wolf R. N. et al., 2013, Phys. Rev. Lett. 110, 041101
Yakovlev D. G., Pethick C. J., 2004, ARA&A 42, 169
Yakovlev D. G., Levenfish K. P., Shibanov Yu. A., 1999, Phys. Usp. 42, 737
Yakovlev D. G., Kaminker A. D., Gnedin O. Y., Haensel P., 2001, Phys. Rep. 354, 1
Zhou P., Chen Y., Li X.-D., Safi-Harb S., Mendez M., Terada Y., Sun W., Ge M.-Y., 2014, ApJ 781, L16